

Lawrence Berkeley National Laboratory

LBL Publications

Title

Crossover from 2D Ferromagnetic Insulator to Wide Band Gap Quantum Anomalous Hall Insulator in Ultrathin MnBi₂Te₄

Permalink

<https://escholarship.org/uc/item/3g03105d>

Journal

ACS Nano, 15(8)

ISSN

1936-0851

Authors

Trang, Chi Xuan

Li, Qile

Yin, Yuefeng

et al.

Publication Date

2021-08-24

DOI

10.1021/acsnano.1c03936

Peer reviewed

Crossover from 2D ferromagnetic insulator to wide bandgap quantum anomalous Hall insulator in ultra-thin MnBi_2Te_4

Chi Xuan Trang[#], Qile Li[#], Yuefeng Yin[#], Jinwoong Hwang, Golrokh Akhgar, Iolanda Di Bernardo, Antonija Grubišić-Čabo, Anton Tadich, Michael S. Fuhrer, Sung-Kwan Mo, Nikhil V. Medhekar^{*}, Mark T. Edmonds^{*}

[#] These authors contributed equally

^{*} Corresponding author: mark.edmonds@monash.edu and nikhil.medhekar@monash.edu

Abstract

Intrinsic magnetic topological insulators offer low disorder and large magnetic bandgaps for robust magnetic topological phases operating at higher temperatures. By controlling the layer thickness, emergent phenomena such as the quantum anomalous Hall (QAH) effect and axion insulator phases have been realized. These observations occur at temperatures significantly lower than the Néel temperature of bulk MnBi_2Te_4 , and measurement of the magnetic energy gap at the Dirac point in ultra-thin MnBi_2Te_4 has yet to be achieved. Critical to achieving the promise of this system is a direct measurement of the layer-dependent energy gap and verification of a temperature-dependent topological phase transition from large bandgap QAH insulator to a gapless TI paramagnetic phase. Here we utilize temperature-dependent angle-resolved photoemission spectroscopy to study epitaxial ultra-thin MnBi_2Te_4 . We directly observe a layer-dependent crossover from a 2D ferromagnetic insulator with a bandgap greater than 780 meV in one septuple layer (1 SL) to a QAH insulator with a large energy gap (>70 meV) at 8 K in 3 and 5 SL MnBi_2Te_4 . The QAH gap is confirmed to be magnetic in origin, as it becomes gapless with increasing temperature above 8 K.

Keywords: magnetic topological insulator, thin film, MnBi_2Te_4 , quantum anomalous Hall insulator, ferromagnetic insulator, angle-resolved photoemission spectroscopy.

Introduction

Topological insulators (TIs) in three-dimensions possess a topologically protected spin-polarized gapless Dirac cone on the surface of a bulk insulator that is robust against time-reversal invariant perturbations.¹⁻⁷ Time-reversal symmetry in TIs can be broken by introducing long-range magnetic order, resulting in profound changes to the electronic band structure, specifically a gap opening at the Dirac point caused by exchange coupling.^{6,8-10} The combination of magnetization and strong spin-orbit coupling in ultra-thin topological insulators not only results in a gap opening but also the presence of chiral edge modes within the magnetic gap representing the quantum anomalous Hall (QAH) insulating state.⁹⁻¹¹ In this state the edge mode is chiral and perfectly spin polarized, yielding dissipationless transport of charge with applications in spintronic and ultra-low energy electronics.¹² Further, a realization of distinct topological phases based on broken time-reversal symmetry such as the chiral Majorana fermion¹³ and axion insulator states are also achievable.^{14,15}

The QAH effect was first realized *via* dilute magnetic doping using Cr and V in ultra-thin films of $(\text{Bi,Sb})_2\text{Te}_3$.^{9,10} However, the non-uniform doping and magnetization result in large spatial fluctuations in the size of the magnetic gap,¹⁶ and the parallel dissipative channels create spin-scattering which greatly suppresses the temperature at which QAH effect can be observed. Modulation-doped sandwich heterostructures have modestly raised the QAHE temperature to 1-2 K,^{17,18} which is still far below the size of the magnetic gap and the Curie temperature. To explore the QAHE and other topological phases at elevated temperatures requires uniform distribution of magnetization, not readily achieved *via* dilute magnetic doping.

The intrinsic magnetic topological insulator MnBi_2Te_4 was recently proposed¹⁹⁻²² and experimentally verified as a bulk antiferromagnetic topological insulator²³⁻²⁶ that hosts both intrinsic magnetism and topological protection. MnBi_2Te_4 is a layered compound similar to the well-known TI Bi_2Te_3 , where five atomic layers of Te - Bi - Te - Bi - Te form a quintuple layer (QL), however, MnBi_2Te_4 has an extra Mn - Te layer in between Te and Bi in the middle of the Bi_2Te_3 quintuple layer, forming a septuple layer (SL) (Fig. 1a). The origin of the magnetic order comes from the Mn^{2+} ions (contributing a $5 \mu_B$ magnetic moment), with moments coupled ferromagnetically within each SL, and antiferromagnetically between adjacent SLs, resulting in an uncompensated antiferromagnet. By controlling the layer structure in the 2D limit a set of thickness-dependent magnetic and topological transitions have been predicted, such as a

1
2
3 wide bandgap ferromagnetic (FM) insulator in 1 SL with potential applications in proximity-
4 induced magnetization.²¹ Beyond 1 SL, even- and odd-layered systems are predicted to be
5 axion insulators and wide-bandgap QAH insulators respectively.^{19,22} Recent transport
6 experiments on MnBi_2Te_4 have confirmed the axion insulator phase in 6 SL¹⁵ and the QAHE
7 in 5 SL at 1.4 K at zero magnetic field, further increased to 6.5 K in an external magnetic field
8 by aligning the layers ferromagnetically.²⁷ Yet these temperatures correspond to thermal
9 energies < 1 meV and are still well below the predicted magnetic bandgap values (ranging
10 between 38 meV¹⁹ and 98 meV²⁷) and below the Néel temperature ($T_N \approx 23\text{-}25$ K^{25,27}). To date,
11 the electronic bandstructure of ultra-thin MnBi_2Te_4 has only been examined above the Néel
12 temperature where it appears gapless.²⁸ Hence there has been no direct confirmation of the
13 crossover from ferromagnetic (FM) insulator to QAH insulator with increasing layer thickness,
14 nor a direct observation of the size or magnetic nature of the energy gap in the QAH state.

15
16
17 In this work we precisely control the layer thickness of MnBi_2Te_4 *via* molecular beam
18 epitaxy growth (MBE) and perform temperature-dependent angle-resolved photoelectron
19 spectroscopy (ARPES) above and below the Néel temperature to reveal the layer-dependent
20 crossover from 2D ferromagnetic insulator ($\Delta_{\text{GAP}} > 780$ meV) in 1 SL to QAH insulator with
21 large gaps ($\Delta > 70$ meV at 8 K) in 3 and 5 SL, in excellent agreement with first-principles
22 density functional theory (DFT) calculations. The QAH gap is confirmed to be magnetic in
23 origin, as it abruptly becomes zero with increasing temperature as the system becomes
24 paramagnetic, demonstrating a phase transition from QAH insulating state to topological
25 gapless surface state.

26 27 28 29 30 31 32 33 34 35 36 37 38 39 40 41 42 **Results and Discussion**

43
44
45 High-quality MnBi_2Te_4 films were grown by molecular beam epitaxy on $\text{Si}(111)\text{-}7 \times 7$
46 substrates *via* alternately growing 1 QL Bi_2Te_3 and 1 BL MnTe to spontaneously form
47 MnBi_2Te_4 (see Methods for specific details on the growth). Figure 1b shows a Reflection High-
48 energy Electron Diffraction (RHEED) pattern of 3 SL MnBi_2Te_4 . The atomically flat
49 morphology of the film is indicated by a sharp (1×1) streak pattern (see SI Section 1 for LEED
50 and additional RHEED data). Figure 1c shows an atomic-resolution scanning tunneling
51 microscopy (STM) image and the expected 1×1 atomic structure with a lattice constant of 4.3
52 Å. A constant binding energy ARPES map taken at the Fermi level (*i.e.* Fermi surface map) of
53 2 SL MnBi_2Te_4 , capturing multiple Brillouin zones (BZ) is shown in Fig. 1d. In each BZ, the
54
55
56
57
58
59
60

only features observed are at the $\bar{\Gamma}$ points, showing a slight hexagonal warping of the Fermi surface. The hexagonal features confirm threefold rotational symmetry, consistent with the rhombohedral structure of MnBi_2Te_4 . An in-plane lattice constant, $a \approx 4.3 \text{ \AA}$ can be calculated from the Fermi surface map for 2 SL, with similar values for 3 and 5 SL (see SI Section 2) in excellent agreement with STM (Fig. 1c) and previous reports on bulk MnBi_2Te_4 .^{26,29} In contrast, 1 SL has a lattice constant of 4.06 \AA suggesting there is the compressive strain when in direct contact with the Si(111), immediately relaxed when the thickness increases. These results are summarized in Table 1. Figure 1e shows x-ray photoelectron spectroscopy (XPS) of 5 SL taken at $h\nu = 1486 \text{ eV}$, with the characteristic Mn $3p$, Te $4d$ and Bi $5d$ core levels observed in the correct chemical stoichiometry when accounting for the different photoionization cross sections. Depth dependent XPS measurements are shown in Fig. S3 to demonstrate the films are composed of solely MnBi_2Te_4 and not a composition of Bi_2Te_3 with MnTe on the top.

By delicate control of the growth conditions, we achieve SL-by-SL growth of MnBi_2Te_4 , allowing the DFT-predicted transition from ferromagnetic insulator to quantum anomalous Hall insulator to be probed directly with ARPES. The upper panel of Figure 2 shows a series of ARPES band maps of MnBi_2Te_4 with thicknesses of (a) 1 SL, (b) 2 SL, (c) 3 SL and (d) 5 SL measured along the $\bar{\Gamma}\bar{M}$ direction. The middle panel in Fig. 2 plots the respective double derivative, and the bottom panel plots the corresponding DFT calculations using HSE functional (1-3 SL) and PBE functional (5 SL). There is a clear thickness-dependent transition from wide-bandgap in 1 SL (Fig. 2a) to an evolution into nearly Dirac-like dispersion in 3 and 5 SL (Fig. 2c-d), evidence of evolution towards non-trivial topological features. There is an excellent overlap with the DFT calculations in the overall band shape and with increasing thickness, along with a rigid shift in the bands toward the Fermi level, suggesting the film becomes less n -type due to increased manganese content which acts as a hole dopant.⁶

In Fig. 3a-b we determine the bandgap in 1 and 2 SL MnBi_2Te_4 respectively, by plotting the ARPES spectrum (left panel), its double derivative (middle panel) and the corresponding energy distribution curves (right panel). In Fig. 3a the ARPES spectrum of 1 SL MnBi_2Te_4 exhibits only a broad M-shaped valence band (VB), with the valence band maximum $\approx 780 \text{ meV}$ below the Fermi level, with no signature of the conduction band (CB) and a strong intensity bulk Si(111) band observed below 1.1 eV . The overall band shape confirms an indirect bandgap ferromagnetic insulator in excellent agreement with our DFT results and Ref.

22. This is different from that reported by Ref. 19 which reports a direct bandgap, which is likely as a result of applying the on-site Hubbard correction term to Te instead of Mn (further discussion and calculations are found in Section S4 of the SI). The gap >780 meV is larger than theoretical predictions (see Table 1) and is either due to bandgap underestimation in DFT³⁰ or the compressive strain that is observed in 1SL. The gap size is comparable to other 2D ferromagnets, such as monolayer CrI₃,³¹ but is significantly larger than in (non-magnetic) 1 QL pristine Bi₂Te₃.⁴ In Fig. 3b for the 2 SL film the M-shaped VB is preserved but now a parabolic CB appears, whose minimum is below E_F , indicating the film is *n*-type doped. The CB dispersion within a 0.15 \AA^{-1} region extending from the $\bar{\Gamma}$ point is fit using a nearly free electron model, $E = \hbar^2 k^2 / 2m^*$, yielding an effective mass, $m^* = 0.25 m_0$ (see Section S5 and Fig. S7 in SI for fits). An extremely weak intensity hole band, only observable when taking a double derivative (middle panel of Fig. 3b), results in a direct bandgap of 300 ± 100 meV. The excellent agreement with DFT suggests that 2 SL is a zero plateau QAH insulator.²²

We now examine the size of the bandgap in 3 SL and 5 SL MnBi₂Te₄. Figure 4a shows high-resolution ARPES maps taken at $h\nu = 50$ eV and 8 K (*i.e.* well below the Néel temperature, $T_N \approx 23\text{-}25$ K^{25,27}) for 3 SL (top panel) and 5 SL (bottom panel). The red circles overlaid reflect the extracted maxima from fitting momentum distribution curves (MDC) with Lorentzian line shapes in the k range between -0.5 to $+0.5 \text{ \AA}^{-1}$ as shown in Fig. 4b. Fitting with four-line shapes was used for binding energies below ~ 0.4 eV and ~ 0.3 eV for 3 SL and 5 SL respectively, in order to decouple the linearly dispersing Dirac bands from additional valence bands which are clearly present in the MDCs in Fig. 4b and predicted in the DFT calculations in Fig. 4c. These additional bands when interacting with the Dirac hole band lead to an anti-crossing and manifest as a slight kink in the band dispersion. The strong spectral weight near $\bar{\Gamma}$ in the Dirac point region is due to Te-orbital-related matrix element effects (see Fig. S6 for orbital character analysis) as this intensity diminishes quickly with changing photon energy (see Fig. S8). This strong spectral weight has previously been observed in the Dirac point region of Bi₂Te₃³ and Bi₂Te₃/MnBi₂Te₄ heterostructures, but not in Mn-doped Bi₂Se₃.⁷ A clear electron and hole band asymmetry is observed, yielding asymptotic Fermi velocities for 3 SL of $v_{F,e} \approx 4.2 \times 10^5 \text{ ms}^{-1}$ and $v_{F,h} \approx 2.0 \times 10^5 \text{ ms}^{-1}$ and for 5 SL $v_{F,e} \approx 5.0 \times 10^5 \text{ ms}^{-1}$ and $v_{F,h} \approx 2.9 \times 10^5 \text{ ms}^{-1}$. The hole band v_F for both 3 SL and 5 SL was extracted above the kink regions discussed above.

The band dispersion for both 3 SL and 5 SL appear hyperbolic as expected for a massive Dirac dispersion, and the linear extrapolation of the electron and hole bands to $k = 0$ shows the bands do not meet at a discrete point (*i.e.* the Dirac point) but are actually separated by 40 ± 15 meV for both 3 SL and 5 SL MnBi₂Te₄. This strongly supports the conclusion that the system is gapped, and in order to accurately determine the size of the bandgap we utilize two independent methods. The first is based on the hyperbolic band dispersion for both 3 SL and 5 SL as expected for a massive Dirac dispersion, so we fit the data to a model of a hyperbolic system (shown as white bands in Fig. 4a) given by

$$E_i(k) = D \pm \sqrt{\Delta_i^2 + \hbar^2 v_{F,i}^2 (k + k_0)^2}, i \in n,p \quad (1)$$

where $\Delta = \Delta_n + \Delta_p$ represents the bandgap, D the doping, and $v_{F,i}$ the asymptotic Fermi velocities away from the gapped region at large momenta. This yields magnetic gap sizes of $\Delta_{3\text{SL}} = 109 \pm 15$ meV and $\Delta_{5\text{SL}} = 84 \pm 15$ meV. Figure 4c overlays the DFT band calculations and shows excellent overlap for 3 SL, whilst the 5 SL PBE (due to underestimation of the bandgap³⁰) required the bandgap to be adjusted to match the experimental data using the scissors method.

A check on the determination of the bandgap was performed by peak fitting analysis of the energy distribution curves (EDCs) taken at $k_{\parallel} = 0$. The EDCs for 3 SL and 5 SL MnBi₂Te₄ taken at 8 K are plotted in Fig. 4d, along with the peak fitting analysis based on Ref. 7 for Bi₂Te₃/MnBi₂Te₄ heterostructures where a pronounced shoulder is observed when cooling below 13 K (the temperature dependence and the evolution of electronic structure is shown in Fig. 5 and discussed in detail below). We fit the dominant spectral weight with two identical Lorentzian line shapes, and include small additional conduction and valence band peaks either side of the main peaks that reflect the electron and hole Dirac bands. At 8 K we arrive at gaps for 3 SL and 5 SL of 71 ± 15 meV and 70 ± 15 meV respectively. In Fig. S11 of the SI we include fits of the 8 K data with: (a) four peaks to reflect a gapped system and (b) three peaks to reflect a gapless system with only a single main Dirac peak. The three peaks fit is unable to reproduce the shoulder on the right flank of the peak in the experimental data, validating our four peak fitting approach. The bandgap derived from EDC fitting using four peak components shows excellent agreement with that obtained from fitting to Eqn. (1) for 5 SL MnBi₂Te₄ and slight discrepancy above experimental error for 3 SL. Figure 4e plots the bandgap as a function of thickness for experiment and DFT calculations from this work and that of Ref. 22, and are also summarised in Table 1.

1
2
3 We now investigate the response of the topological electronic structure to magnetic
4 ordering, by conducting temperature-dependent ARPES measurements. Figure 5a shows the
5 energy distribution curves at $k_{\parallel} = 0$ measured at temperature $T = 8$ K and 13 K for 5 SL
6 MnBi_2Te_4 . There is a clear broadening upon cooling from 13 K, and the right flank of the peak
7 (*i.e.* lower binding energy) develops a clear shoulder. Higher temperature measurements (up to
8 33 K) show minimal change from the 13 K data, which suggests that 8 K is below the magnetic
9 phase transition temperature, *i.e.* uncompensated antiferromagnetic phase (uAFM), and 13 K
10 above it, *i.e.* paramagnetic phase. In Fig. 5b we fit the $T = 13$ K spectra (fitting up to 33 K was
11 also performed) with two almost identical components yielding a splitting of 15 meV. Figure
12 S11 in the SI shows a comparison between fitting with: (c) two peaks and (d) on peak
13 component at 13 K. A slightly larger peak intensity for the hole band was adopted due to the
14 lower Fermi velocity of the hole band. This splitting of less than 15 meV reflects a nearly
15 gapless topological insulator (that maintains a small remnant confinement gap due to its ultra-
16 thin nature) confirming the system is now paramagnetic. The sum of these two peaks is plotted
17 as a single peak component (red line shape) for clarity in Fig. 5b. Upon cooling to 8 K and the
18 uAFM phase, the peak splitting of these two components (blue line shapes) increases and yields
19 a magnetic gap, $\Delta = 70 \pm 15$ meV.
20
21
22
23
24
25
26
27
28
29
30
31
32
33

34 There is further evidence of a band evolution between 8 and 13 K when examining the near-
35 E_F ARPES maps and the corresponding MDCs at 8 K (Fig. 5c) and 13 K (Fig. 5d) (full
36 temperature range 8-33 K is shown in Fig. S9). As shown in Fig. 5e at binding energies, $E_B =$
37 0, 0.25, and 0.36 eV there is a clear increase in wavevector, k with increasing T . However, the
38 slope of the electron and hole band (and consequently Fermi velocity) extracted from the MDC
39 maxima remains unchanged as shown in Fig. S9c of the SI. At 13 K and above linear
40 extrapolation of the bands to $k = 0$ yields a gap $\Delta < 10$ meV in excellent agreement with the
41 EDC analysis above. The near gapless nature at 13 K and above is further confirmed *via*
42 ARPES measurements taken at $T = 13$ K and $h\nu = 40$ eV (shown in Fig. S10) in order to avoid
43 the strong spectral weight of the Te orbital in the gapped region. This clearly shows a gapless
44 Dirac dispersion and is consistent with measurements taken on 5 and 7 SL MnBi_2Te_4 at 25 K
45 in Ref. 28. Figure 5f plots the bandgap as a function of temperature.
46
47
48
49
50
51
52
53
54
55

56 This clear emergence of a magnetization induced gap with decreasing temperature provides
57 a definitive signature for a temperature-dependent topological phase transition from large
58 bandgap QAH insulator to a near gapless TI paramagnetic phase. These phases are depicted
59
60

schematically in Fig. 5g. It should be noted the phase transition temperature reported here between 8-13 K is well below the $T_N \approx 23$ K reported for 5 SL MnBi_2Te_4 ²⁷ however, in both Ref. 22 and 27 a decrease in the Néel temperature is reported with decreasing thickness. Furthermore, Ref. 27 reports corrections to the temperature dependent resistivity with an abrupt downturn in resistivity below T_N , followed by a rapid increase at ≈ 10 K which they attribute to localization. The abrupt transition observed at similar temperature here in ARPES, along with the QAH effect in MnBi_2Te_4 being limited to 6.5 K²⁷, suggests that the phase transition responsible for topological order may occur below the Néel temperature (indicating more than one magnetic phase transition) or the Néel temperature may be lower in these samples than previously thought and further work is needed to understand this behavior and also to understand whether there are spatial variations in the bandgap due to magnetic disorder, which has been previously observed in dilute magnetically doped TI's.¹⁶

Conclusions

Our results provide an experimental demonstration of the thickness-dependent electronic properties of MnBi_2Te_4 , from a wide bandgap 2D ferromagnet to a QAH insulator with a magnetic bandgap in excess of 70 meV. Therefore, MnBi_2Te_4 not only offers pathways to realise high temperature QAH effect but is also applicable in designer van der Waals heterostructures for proximity induced magnetization²¹ and in the realization of distinct topological phases such as chiral Majorana fermions *via* coupling to a superconductor.¹³

Methods

Growth of Ultra-Thin MnBi_2Te_4 on Si(111)

Ultra-thin MnBi_2Te_4 thin films were grown in an ultra-high vacuum (UHV) molecular beam epitaxy (MBE) chamber and then immediately transferred after the growth to an interconnected ARPES chamber at Beamline 10.0.1, Advanced Light Source (ALS), Lawrence Berkeley National Laboratory, USA. To prepare an atomically flat substrate, a Si(111) wafer was flash annealed with e-beam heating in order to achieve a (7×7) surface reconstruction.

For MnBi_2Te_4 film growth, effusion cells were used to evaporate elemental Bi (99.999%) and Mn (99.9%) in an overflux of Te (99.95%). Rates were calibrated with a quartz crystal microbalance. High quality epitaxial growth of MnBi_2Te_4 was achieved by first growing 1QL

1
2
3 of Bi_2Te_3 at 230°C , then a bilayer of MnTe was deposited in order to spontaneously form
4 MnBi_2Te_4 in a similar manner to the formation of MnBi_2Se_4 ¹. To reach the desired thickness
5 this recipe was continued by again depositing 1 QL of Bi_2Te_3 followed by a bilayer of MnTe.
6 After growth was completed the film was annealed at the same temperature in an overflux of
7 Te for 5 - 10 min to improve crystallinity. Reflection High Energy Electron Diffraction
8 (RHEED) and Low Energy Electron Diffraction (LEED) were used to confirm the (001) single-
9 crystal epitaxial growth across a large area (see Supplementary Materials S1).

16 **Angle resolved photoemission spectroscopy (ARPES) measurements and x-ray** 17 **photoelectron spectroscopy (XPS)**

20
21 ARPES measurements were performed at Beamline 10.0.1 of the ALS. Data was taken using
22 a Scienta R4000 analyser at temperatures between 8 K and 33 K. The total energy resolution
23 was 15 - 25 meV depending on the beamline slit widths and analyser settings, and the angular
24 resolution was 0.2° . This resulted in an overall momentum resolution of $\approx 0.01 \text{ \AA}^{-1}$ for the
25 photoelectron kinetic energies measured, with the majority of the measurements performed at
26 $h\nu = 50 \text{ eV}$. XPS measurements were performed at the Soft X-ray Beamline of the Australian
27 Synchrotron using a SPECS Phoibos-150 Spectrometer at room temperature. The Bi $5d$, Te $4d$
28 and Mn $3p$ core levels were measured at photon energies of 100 eV, 350 eV, 850 eV and 1486
29 eV. This ensured surface sensitivity for the low photon energy scans at 100 eV, with the higher
30 photon energies used to characterize the depth dependence of the core levels, to confirm there
31 was only MnBi_2Te_4 throughout the film. The binding energy scale of all spectra are referenced
32 to the Fermi energy (E_F), determined using either the Fermi edge or $4f$ core level of an Au
33 reference foil in electrical contact with the sample.
34
35
36
37
38
39
40
41
42
43
44

45 **Density Functional Theory Calculations**

46
47 We employed density functional theory (DFT) calculations as implemented in the Vienna
48 *ab Initio* Simulation Package (VASP) to calculate the electronic structure of two-dimensional
49 MnBi_2Te_4 ². The electron exchange and correlation effects were treated with the Perdew-Burke-
50 Ernzerhof (PBE) form of the generalized gradient approximation (GGA).³ The kinetic energy
51 cut-off for the plane-wave basis was set to 400 eV. We use a $12 \times 12 \times 1$ Γ -centered k -point
52 mesh for sampling the Brillouin zone. The van der Waals interactions in the system is described
53 using the DFT-D3 potential.⁴ To treat the strong, onsite Coulombic interactions of localized $3d$
54 electrons of Mn, which is inaccurately described by GGA, we used GGA+U approach with the
55
56
57
58
59
60

1
2
3 effective Hubbard-like term U set to 4 eV.⁵ The electronic bandstructure of 2D MnBi_2Te_4
4 obtained from PBE-GGA was further verified using the hybrid Heyd-Scuseria-Ernzerhof
5 (HSE) hybrid functional.⁶
6
7

8 9 ASSOCIATED CONTENT

10
11 Preprint version of this manuscript: Chi Xuan Trang; Qile Li; Yuefeng Yin; Jinwoong
12 Hwang; Golrokh Akhgar; Iolanda Di Bernardo; Antonija Grubišić-Čabo; Anton
13 Tadich; Michael S. Fuhrer; Sung- Kwan Mo; Nikhil V. Medhekar; Mark T. Edmonds.
14 Crossover From 2D Ferromagnetic Insulator to Wide Bandgap Quantum anomalous Hall
15 insulator in ultra-thin MnBi_2Te_4 , **2021**, arXiv:2009.06175v2, <https://arxiv.org/abs/2009.06175>
16
17
18
19
20

21 The Supporting Information is available free of charge at (link)

22
23 Sample characterization with LEED and RHEED, lattice constant as a function of
24 thickness, x-ray photoelectron spectroscopy of MnBi_2Te_4 , DFT calculations, effective mass in
25 2 SL, photon energy dependence of 5 SL, temperature dependence of 5 SL, photon-energy
26 dependent gap of 5 SL, a comparison between four peak and three peak fittings.
27
28
29
30
31

32 AUTHOR INFORMATION

33
34
35 **Author contributions** M.T.E. devised the experiments. Q. L., C. X. T., G. A performed the
36 MBE growth at Monash University. C. X. T., Q. L., M.T.E., A. G. C., and I. B. performed the
37 MBE growth and ARPES measurements at the ALS with the support from J.H. and S.-K.M. I.
38 B. performed the STM measurements at Monash University. The DFT calculations were
39 performed by Y. Y., and N. M. C. X. T., Q. L., and M.T.E. composed the manuscript. All
40 authors read and contributed feedback to the manuscript.
41
42
43
44
45

46 ACKNOWLEDGMENTS

47
48
49 M.T.E. was supported by ARC DECRA fellowship DE160101157. M.T.E., C.X.T., Q.L., Y.
50 Y., I. B., G. A., N. M., M.S.F. acknowledge funding support from CE170100039. M.T.E. and
51 C.X.T. acknowledge travel funding provided by the International Synchrotron Access Program
52 (ISAP) managed by the Australian Synchrotron, part of ANSTO, and funded by the Australian
53 Government. M.T.E., C.X.T., and Q.L. acknowledge funding support from ARC Centre for
54 Future Low Energy Electronics Technologies (FLEET). Y.Y. and N.V.M. are thankful for the
55 computational support provided by the Monash Computing Cluster, the National Computing
56
57
58
59
60

1
2
3 Infrastructure and the Pawsey Supercomputing Facility. This research used resources of the
4 Advanced Light Source, which is a DOE Office of Science User Facility under contract no.
5 DE-AC02-05CH11231. Part of this research was also undertaken on the Soft X-ray beamline
6 at the Australian Synchrotron, part of ANSTO.
7
8
9

10
11 **Competing interests** The authors declare no competing interests.
12

13 **References**

- 14
15
16 1. Fu, L.; Kane, C. L.; Mele, E. J. Topological Insulators in Three Dimensions. *Phys. Rev. Lett.*
17 **2007**, *98* (10), 106803.
18
19
- 20
21 2. Hasan, M. Z.; Kane, C. L. Colloquium: Topological Insulators. *Rev. Mod. Phys.* **2010**, *82* (4),
22 3045.
23
24
- 25
26 3. Chen, Y. L.; Analytis, J. G.; Chu, J.-H.; Liu, Z. K.; Mo, S.-K., Qi, X. L.; Zhang, H. J.; Lu, D.
27 H.; Dai, X. ; Fang, Z. ; Zhang, S. C.; Fisher, I. R.; Hussain, Z. ; Shen, Z.-X. Experimental
28 Realization of a Three-Dimensional Topological Insulator, Bi_2Te_3 . *Science* **2009**, *325* (5937),
29 178.
30
31
32
- 33
34 4. Li, Y.-Y., Li, Y.-Y.; Wang, G.; Zhu, X.-G.; Liu, M.-H.; Ye, C.; Chen, X.; Wang, Y.-Y.; He,
35 K.; Wang, L.-L.; Ma, X.-C.; Zhang, H.-J.; Dai, X.; Fang, Z.; Xie, X.-C.; Liu, Y.; Qi, X.-L.;
36 Jia, J.-F.; Zhang, S.-C.; Xue, Q.-K. Intrinsic Topological Insulator Bi_2Te_3 Thin Films on Si
37 and Their Thickness Limit. *Adv. Mater.* **2010**, *22* (36), 4002.
38
39
40
- 41
42 5. Zhang, Y., He, K.; Chang, C.-Z.; Song, C.-L.; Wang, L.-L.; Chen, X.; Jia, J.-F.; Fang, Z.; Dai,
43 X.; Shan, W.-Y.; Shen, S.-Q.; Niu, Q.; Qi, X.-L.; Zhang, S.-C.; Ma, X.-C.; Xue, Q.-K.
44 Crossover of the Three-Dimensional Topological Insulator Bi_2Se_3 to the Two-Dimensional
45 Limit. *Nat. Phys.* **2010**, *6*, 584.
46
47
48
- 49
50 6. Chen, Y. L., Chu, J.-H.; Analytis, J. G.; Liu, Z. K.; Igarashi, K.; Kuo, H.-H.; Qi, X. L.; Mo,
51 S. K.; Moore, R. G.; Lu, D. H.; Hashimoto, M.; Sasagawa, T.; Zhang, S. C.; Fisher, I. R.;
52 Hussain, Z.; Shen, Z. X. Massive Dirac Fermion on the Surface of a Magnetically Doped
53 Topological Insulator. *Science* **2010**, *329* (5992), 659.
54
55
56
- 57
58 7. Rienks, E. D. L. *et al.*, Large Magnetic Gap at the Dirac Point in $\text{Bi}_2\text{Te}_3/\text{MnBi}_2\text{Te}_4$
59 Heterostructures. *Nature* **2020**, *576*, 423.
60

- 1
2
3 8. Yu, R., Zhang, W.; Zhang, H.-J.; Zhang, S.-C.; Dai, X.; Fang, Z. Quantized Anomalous Hall
4 Effect in Magnetic Topological Insulators. *Science* **2010**, *329* (5987), 61.
5
6
- 7
8 9. Chang, C.-Z. *et al.* Experimental Observation of the Quantum Anomalous Hall Effect in a
9 Magnetic Topological Insulator. *Science* **2013**, *340* (6129), 167.
10
11
- 12 10. Chang, C.-Z., Zhao, W.; Kim, D. Y.; Zhang, H.; Assaf, B. A.; Heiman, D.; Zhang, S.-C.;
13 Liu, C.; Chan, M. H. W. High-Precision Realization of Robust Quantum Anomalous Hall
14 State in a Hard Ferromagnetic Topological Insulator. *Nat. Mater.* **2015**, *14*, 473.
15
16
17
- 18 11. Gambardella, P.; Dallmeyer, A.; Maiti, K.; Malagoli, M. C.; Eberhardt, W.; Kern, K.;
19 Carbone, C. Ferromagnetism in One-Dimensional Monatomic Metal Chains. *Nature* **2002**,
20 *416*, 301.
21
22
23
- 24 12. Tokura, Y.; Yasuda, K.; Tsukazaki, A. Magnetic Topological Insulators. *Nature Rev. Phys.*
25 **2019**, *1*, 126.
26
27
28
- 29 13. He, Q. L. *et al.* Chiral Majorana Fermion Modes in a Quantum Anomalous Hall Insulator–
30 Superconductor Structure. *Science* **2017**, *357* (6348), 294.
31
32
33
- 34 14. Li, R.; Wang, J.; Qi, X.-L.; Zhang, S.-C. Dynamical Axion Field in Topological Magnetic
35 Insulators. *Nat. Phys.* **2010**, *6*, 284.
36
37
38
- 39 15. Liu, C.; Wang, Y.; Li, H.; Wu, Y.; Li, Y.; Li, J.; He, K.; Xu, Y.; Zhang, J.; Wang, Y. Robust
40 Axion Insulator and Chern Insulator Phases in a Two-Dimensional Antiferromagnetic
41 Topological Insulator. *Nat. Mater.* **2020**, *19*, 522.
42
43
44
- 45 16. Lee, I.; Kim, C. K.; Lee, J.; Billinge, S. J. L.; Zhong, R.; Schneeloch, J. A.; Liu, T.; Valla,
46 T.; Tranquada, J. M.; Gu, G.; Davis, J. C. S. Imaging Dirac-Mass Disorder from Magnetic
47 Dopant Atoms in the Ferromagnetic Topological Insulator $\text{Cr}_x(\text{Bi}_{0.1}\text{Sb}_{0.9})_{2-x}\text{Te}_3$. *Proc. Natl*
48 *Acad. Sci. USA* **2015**, *112* (5), 1316.
49
50
51
52
- 53 17. Ou, Y.; Ou, Y.; Liu, C.; Jiang, G.; Feng, Y.; Zhao, D.; Wu, W.; Wang, X.-X.; Li, W.; Song,
54 C.; Wang, L.-L.; Wang, W.; Wu, W.; Wang, Y.; He, K.; Ma, X.-C.; Xue, Q.-K. Enhancing
55 the Quantum Anomalous Hall Effect by Magnetic Codoping in a Topological Insulator. *Adv.*
56 *Mater.* **2018**, *30* (1), 1703062.
57
58
59
60

- 1
2
3 18. Mogi, M.; Yoshimi, R.; Tsukazaki, A.; Yasuda, K.; Kozuka, Y.; Takahashi, K. S.; Kawasaki,
4 M.; Tokura, Y. Magnetic Modulation Doping in Topological Insulators Toward Higher-
5 Temperature Quantum Anomalous Hall Effect. *Appl. Phys. Lett.* **2015**, *107*, 182401.
6
7
8
9
10 19. Li, J.; Li, Y.; Du, S.; Wang, Z.; Gu, B.-L.; Zhang, S.-C.; He, K.; Duan, W.; Xu, Y. Intrinsic
11 Magnetic Topological Insulators in Van der Waals Layered MnBi_2Te_4 -Family Materials. *Sci.*
12 *Adv.* **2019**, *5* (6), eaaw5685.
13
14
15
16 20. Zhang, D.; Shi, M.; Zhu, T.; Xing, D.; Zhang, H.; Wang, J. Topological Axion States in the
17 Magnetic Insulator MnBi_2Te_4 with the Quantized Magnetoelectric Effect. *Phys. Rev. Lett.*
18 **2019**, *122* (20), 206401.
19
20
21
22 21. Otrokov, M. M.; Menshchikova, T. V.; Vergniory, M. G.; Rusinov, I. P.; Vyazovskaya, A.
23 Y.; Koroteev, Y. M.; Bihlmayer, G.; Ernst, A.; Echenique, P. M.; Arnau, A.; Chulkov, E. V.
24 Highly-Ordered Wide Bandgap Materials for Quantized Anomalous Hall and
25 Magnetoelectric Effects. *2D Mater.* **2017**, *4* (2), 025082.
26
27
28
29
30 22. Otrokov, M. M.; Rusinov, I. P.; Blanco-Rey, M.; Hoffmann, M.; Vyazovskaya, A. Yu.;
31 Ereemeev, S. V.; Ernst, A.; Echenique, P. M.; Arnau, A.; Chulkov, E. V. Unique Thickness-
32 Dependent Properties of the Van der Waals Interlayer Antiferromagnet MnBi_2Te_4 Films.
33 *Phys. Rev. Lett.* **2019**, *122* (10), 107202.
34
35
36
37
38 23. Lee, S. H.; Zhu, Y.; Wang, Y.; Miao, L.; Pillsbury, T.; Yi, H.; Kempinger, S.; Hu, J.; Heikes,
39 C. A.; Quarterman, P.; Ratcliff, W.; Borchers, J. A.; Zhang, H.; Ke, X.; Graf, D.; Alem, N.;
40 Chang, C.-Z.; Samarth, N.; Mao, Z. Spin Scattering and Noncollinear Spin Structure-Induced
41 Intrinsic Anomalous Hall Effect in Antiferromagnetic Topological Insulator MnBi_2Te_4 . *Phys.*
42 *Rev. Research* **2019**, *1* (1), 012011(R).
43
44
45
46
47
48 24. Vidal, R.C. *et al.* Surface States and Rashba-type Spin Polarization in
49 Antiferromagnetic MnBi_2Te_4 (0001). *Phys. Rev. B* **2019**, *100* (12), 121104(R).
50
51
52
53 25. Otrokov, M. M. *et al.* Prediction and Observation of an Antiferromagnetic Topological
54 Insulator. *Nature* **2019**, *576*, 416.
55
56
57
58 26. Zeugner, A. *et al.* Chemical Aspects of the Candidate Antiferromagnetic Topological
59 Insulator MnBi_2Te_4 . *Chem. Mater.* **2019**, *31* (8), 2795.
60

- 1
2
3
4
5
6
7
8
9
10
11
12
13
14
15
16
17
18
19
20
21
22
23
24
25
26
27
28
29
30
31
32
33
34
35
36
37
38
39
40
41
42
43
44
45
46
47
48
49
50
51
52
53
54
55
56
57
58
59
60
27. Deng, Y.; Yu, Y.; Shi, M. Z.; Guo, Z.; Xu, Z.; Wang, J.; Chen, X. H.; Zhang, Y. Quantum Anomalous Hall Effect in Intrinsic Magnetic Topological Insulator MnBi_2Te_4 . *Science* **2020**, *367* (6480), 895.
28. Gong, Y. *et al.* Experimental Realization of an Intrinsic Magnetic Topological Insulator. *Chin. Phys. Lett.* **2019**, *36* (7), 076801.
29. Lee, D. S.; Kim, T.-H.; Park, C.-H.; Chung, C.-Y.; Lim, Y. S.; Seo, W.-S.; Park, H.-H. Crystal Structure, Properties and Nanostructuring of a New Layered Chalcogenide Semiconductor, Bi_2MnTe_4 . *Cryst. Eng. Comm.* **2013**, *15*, 5532.
30. Perdew, J. P.; Yang, W.; Burke, K.; Yang, Z.; Gross, E. K. U.; Scheffler, M.; Scuseria, G. E.; Henderson, T. M.; Zhang, I. Y.; Ruzsinszky, A.; Peng, H.; Sun, J.; Trushin, E.; Görling, A. Understanding Band Gaps of Solids in Generalized Kohn–Sham Theory. *Proc. Natl. Acad. Sci. USA* **2017**, *114* (11), 2801.
31. Webster, L.; Yan, J.-A. Strain-Tunable Magnetic Anisotropy in Monolayer CrCl_3 , CrBr_3 , and CrI_3 . *Phys. Rev. B* **2018**, *98* (14), 144411.

Methods

1. Hirahara, T. *et al.* Large-Gap Magnetic Topological Heterostructure Formed by Subsurface Incorporation of a Ferromagnetic Layer. *Nano Lett.* **2017**, 17, 3493.
2. Kresse, G. & Furthmüller, J. Efficiency of *ab Initio* Total Energy Calculations for Metals and Semiconductors Using a Plane-Wave Basis Set. *Comput. Mater. Sci.* **1996**, 6, 15.
3. Perdew, J. P.; Burke, K. & Ernzerhof, M. Generalized Gradient Approximation Made Simple. *Phys. Rev. Lett.* **1996**, 77, 3865.
4. Grimme, S., Antony, J., Ehrlich, S. & Krieg, H. A Consistent and Accurate *ab Initio* Parametrization of Density Functional Dispersion Correction (DFT-D) for the 94 Elements H-Pu. *J. Chem. Phys.* **2010**, 132, 154104.
5. Dudarev, S. L., Botton, G. A., Savrasov, S. Y., Humphreys, C. J. & Sutton, A.P. Electron-Energy-Loss Spectra and the Structural Stability of Nickel Oxide: An LSDA+U Study. *Phys. Rev. B* **1998**, 57, 1505.
6. Heyd, J. & Scuseria, G.E. Hybrid Functionals Based on a Screened Coulomb Potential. *J. Chem. Phys.* **2003**, 118, 8207.

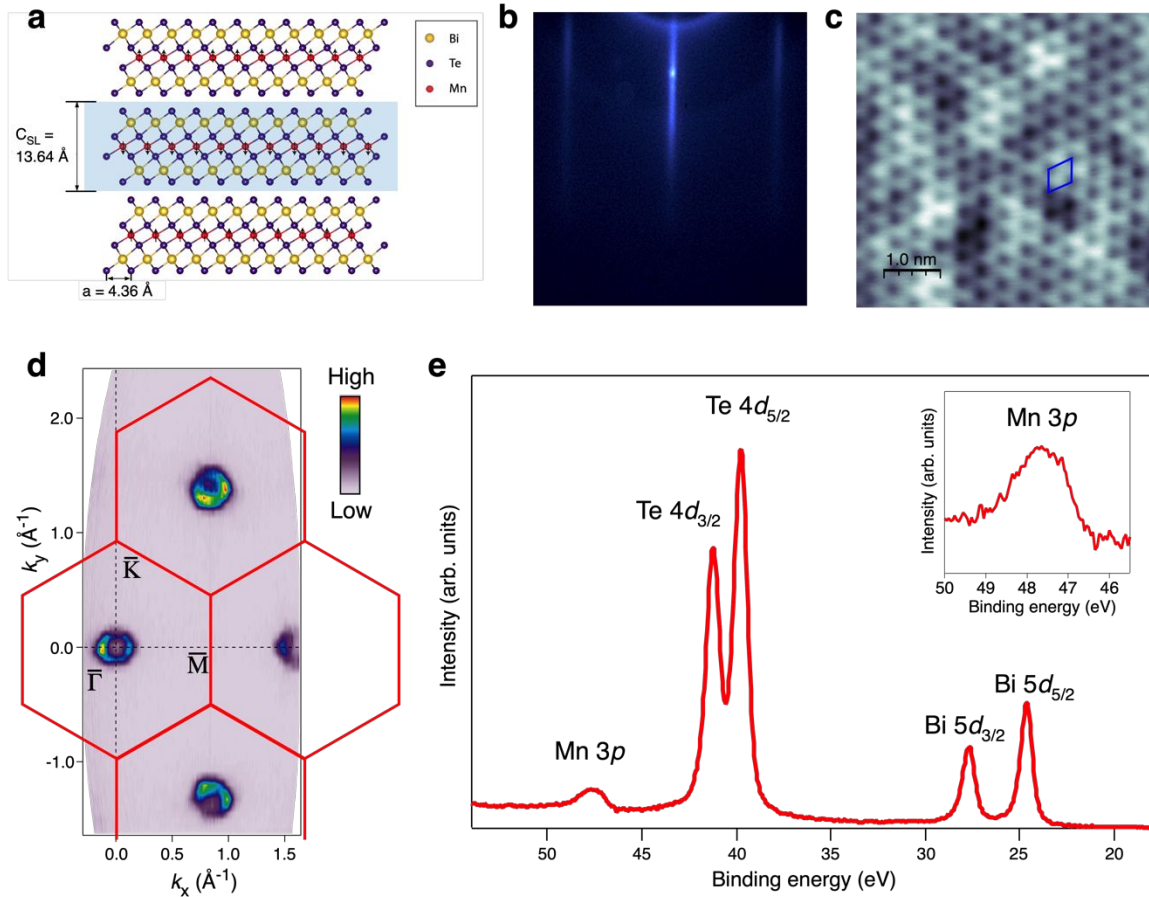


Figure 1 | Basic properties and characterization of MnBi_2Te_4 . **a**, layered crystal structure of MnBi_2Te_4 . **b**, Reflection High-Energy Electron Diffraction (RHEED) of 3 SL MnBi_2Te_4 along [112] direction. **c**, Atomic resolution scanning tunnelling microscope (STM) ($5\text{nm} \times 5\text{nm}$) image of MnBi_2Te_4 ($V = -2.7\text{ V}$, $I = 70\text{ pA}$) showing the 1×1 structure (blue diamond). Lattice constant is 0.43 nm . **d**, Constant energy ARPES contour of 2 SL MnBi_2Te_4 taken at the Fermi level over multiple Brillouin zones (BZ). Hexagonal BZ is overlaid in red. **e**, Core-level spectrum of MnBi_2Te_4 taken at $h\nu = 1486\text{ eV}$ showing the characteristic Mn $3p$, Te $4d$ and Bi $5d$ core levels.

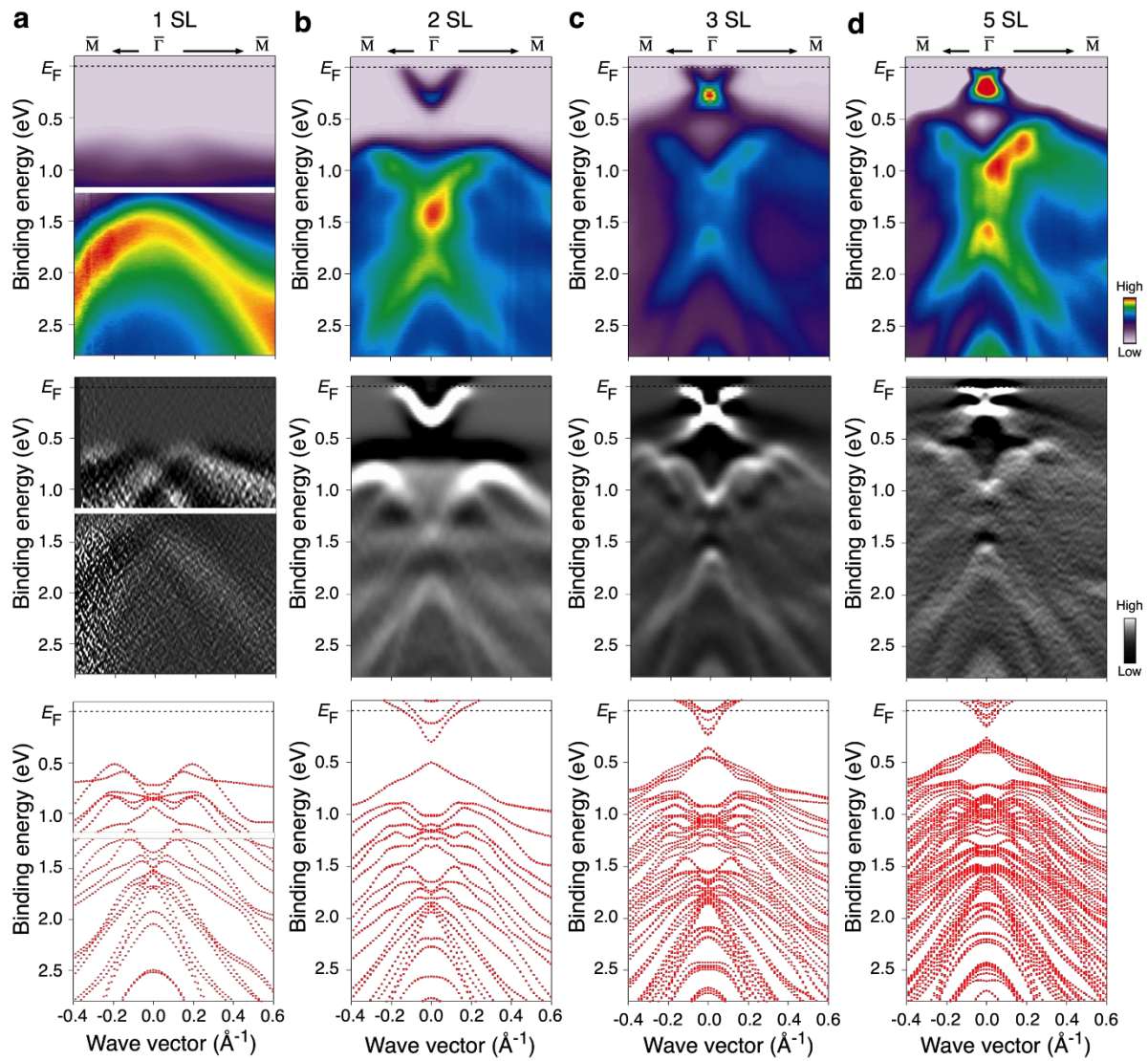


Figure 2 | Thickness dependence of the band structure of MnBi_2Te_4 and comparison with calculation. ARPES intensity (top), double derivatives (middle), and DFT calculation (bottom) of **a**, 1 SL; **b**, 2 SL; **c**, 3 SL; and **d**, 5 SL along $\bar{\Gamma}\bar{M}$ cut, measured at $h\nu = 50$ eV and $T = 13$ K.

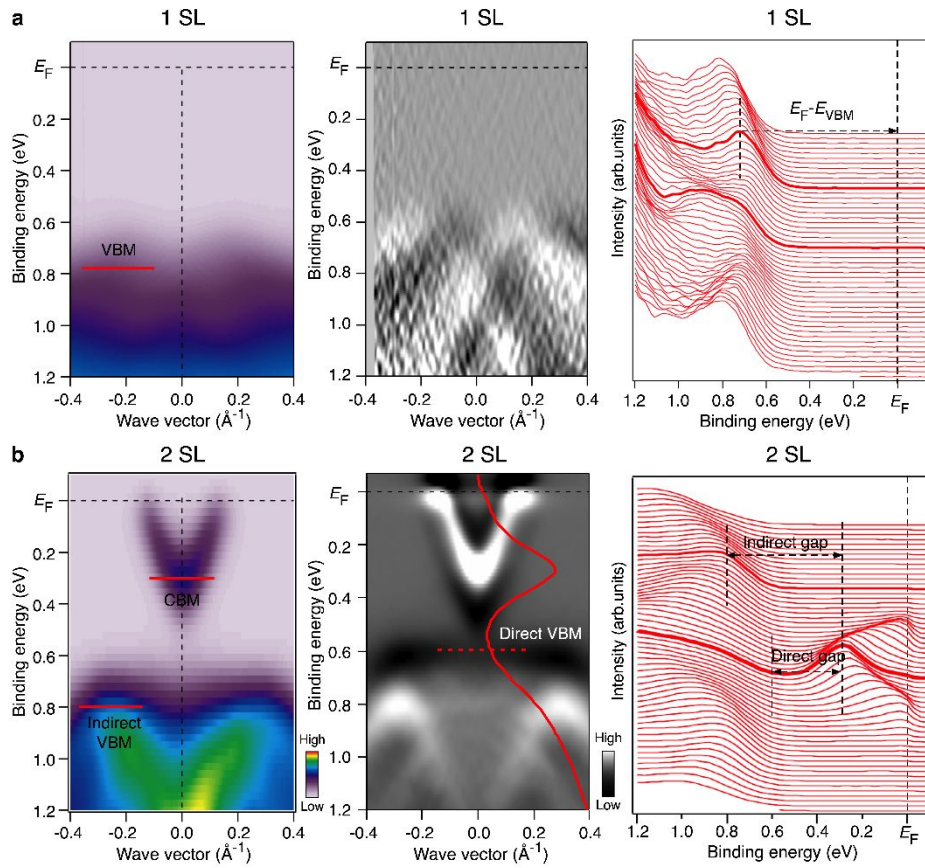


Figure 3 | Bandgap of 1 and 2 SL MnBi_2Te_4 . Near E_F -ARPES intensity (left) at $h\nu = 50$ eV and $T = 12$ K, double derivatives (middle), and corresponding energy distribution curves (EDCs) (right) around the $\bar{\Gamma}$ point for **a**, 1 SL, and **b**, 2 SL. The VB maximum and CB minimum are marked as red lines in ARPES intensity.

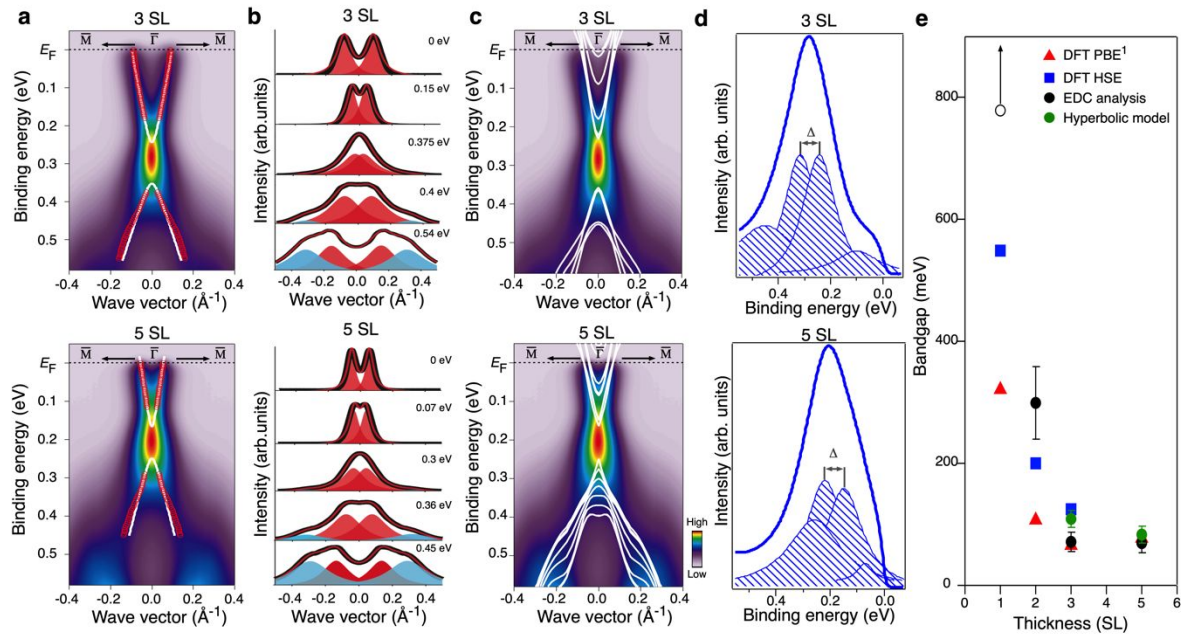


Figure 4 | Magnetic gap of 3 and 5 SL MnBi_2Te_4 . High resolution ARPES intensity of 3 SL (top) and 5 SL (bottom) taken at $h\nu = 50$ eV and $T = 8$ K with overlaid **a**, hyperbolic band fittings (white lines) with extracted momentum distribution curve (MDC) peak maxima (red circles). **b**, MDCs at different E_B fitted with Lorentzian line shapes. **c**, DFT calculations overlaid on the ARPES data. **d**, EDC spectra taken at $k_{\parallel}=0$. The splitting of the two main peak line shapes corresponds to the magnetic gap, Δ . **e**, Bandgap as a function of thickness including data from experiment (black), fittings from Hyperbolic Model (green), DFT calculation (blue), and M. M. Otrokov *et al.*²² (red). The open circle for 1 SL reflects only the E_F-E_{VBM} , and not the bandgap as the conduction band is not observed below the Fermi level.

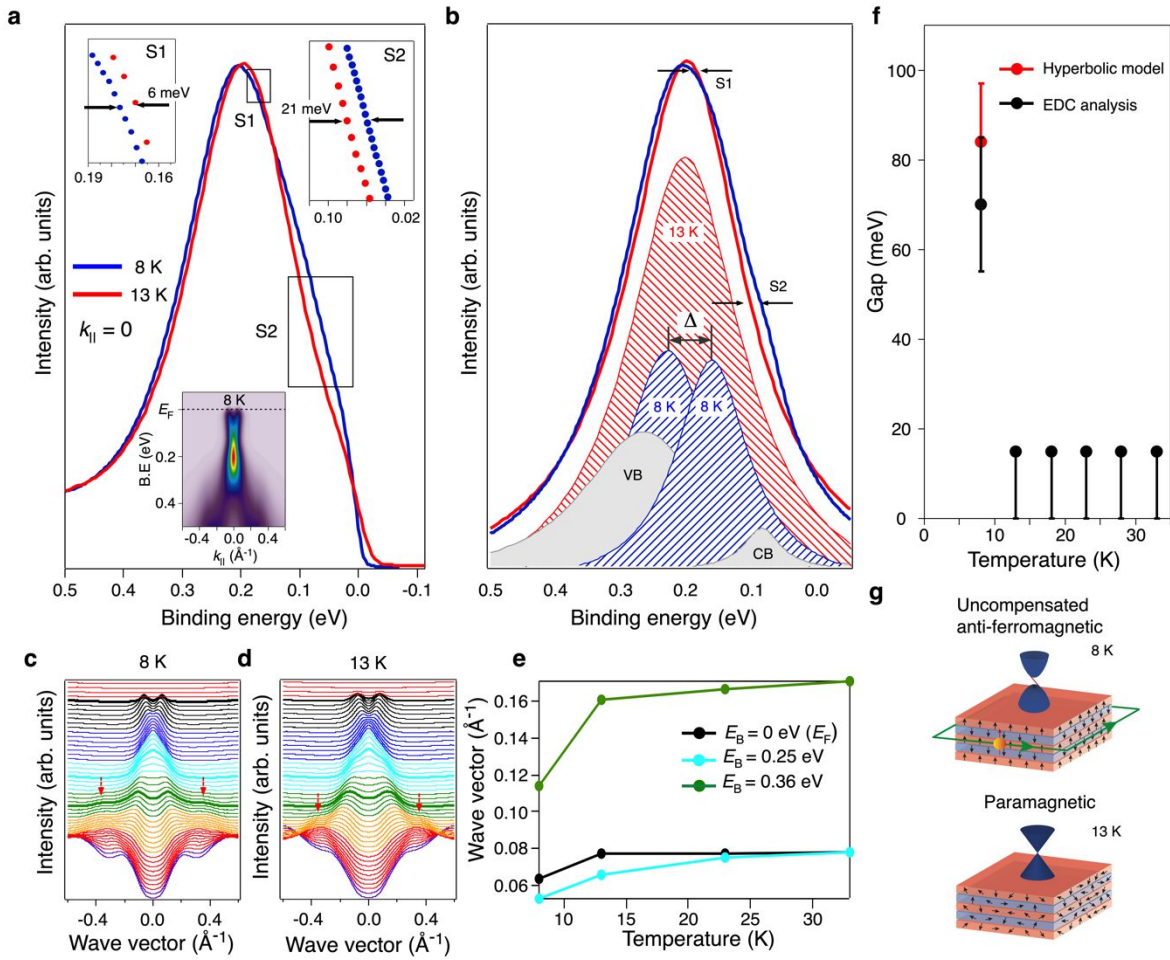


Figure 5| Temperature dependence of 5 SL film. **a**, Energy distribution curves (EDCs) taken at $k_{\parallel}=0$ taken at 8 and 13 K for 5 SL MnBi_2Te_4 . The regions S1 and S2 indicate a clear broadening and pronounced shoulder at 8 K, corresponding to a splitting of 6 meV and 27 meV, respectively. The inset in **a** shows the ARPES map taken at 8 K. **b**, Simulated peak fitting results from the spectra in **a**, corresponds to a magnetic gap of 70 ± 15 meV at 8 K and 15 ± 15 meV at 13 K. **c-d**, MDCs with different colors designating different binding energy regions for 3 SL and 5 SL respectively. Black: $E_F - 0.09$ eV, blue: 0.1-1.9 eV, sky blue: 0.2-0.29 eV, green: 0.3-0.39 eV, orange: 0.4-0.49 eV, red: 0.5-0.59 eV, purple: 0.6-0.62 eV. **e**, Wave vector, k extracted from MDC peak maxima as a function of temperature at $E_B = 0$ (black), 0.25 (blue), 0.36 (green) eV showing a clear band evolution with increasing temperature. **f**, Bandgap as a function of temperature. **g**, Schematics of uncompensated anti-ferromagnetic QAH insulator phase (upper) and paramagnetic gapless TI phase (lower).

Table 1 Lattice constant, bandgap and Fermi velocity as a function of thickness of MnBi₂Te₄

	Lattice constant, a (Å)	E_g (meV) Theory	E_g (meV) Experiment	v_F (m/s) Hole	v_F (m/s) Electron
1 SL	4.06 ± 0.30	550 [this work] 700 [Ref ¹⁹] 321 [Ref ²²]	$>780 \pm 100$	-	-
2 SL	4.31 ± 0.30	200 [this work] 107 [Ref ²²]	300 ± 100	-	-
3 SL	4.31 ± 0.30	125 [this work] 66 [Ref ²²]	109 ± 15 (Hyperbolic Model) 71 ± 15 (EDC Model)	$2.0 \pm 0.5 \times 10^5$	$4.2 \pm 0.5 \times 10^5$
5 SL	4.31 ± 0.30	38 [Ref ¹⁹] 77 [Ref ²²] 98 [Ref ²⁷]	84 ± 15 (Hyperbolic Model) 70 ± 15 (EDC Model)	$2.9 \pm 0.5 \times 10^5$	$5.0 \pm 0.5 \times 10^5$

TOC graphic

